Electric Power Systems Research 237 (2024) 111020

Contents lists available at ScienceDirect

Electric Power Systems Research

journal homepage: www.elsevier.com/locate/epsr

Sensitivity analysis for stability region of inverter-based resources with direct method and real-time simulation setup

Hadis Hosseinpour *, Mohammed Ben-Idris

Department of Electrical and Computer Engineering, Michigan State University, East Lansing, MI 48824, United States of America

ARTICLE INFO

Keywords:
Inverter-based resources
The stability region
Large-signal stability
RTDS
The sum of squares method
Large disturbance

ABSTRACT

Inverter-based resources (IBRs) have become indispensable in power systems due to their numerous environmental and operational advantages, which can contribute to enhancing overall grid reliability and resilience. However, due to their stability limitations, IBRs commonly disconnect from the grid when a grid-side disturbance happens. Therefore, inverters' extensive integration introduces complexities and challenges to power system stability, necessitating the adoption of sophisticated stability assessment tools. One practical approach for assessing large-signal stability involves delineating the system's stability region. Traditionally, two primary methods have been employed for this purpose: time-domain simulation and direct methods. To tackle the stability assessment of IBRs and sensitivity analysis of stability region, this paper introduces a theoretical direct method based on the sum of squares (SOS) method. It provides a Hardware-in-the-Loop (HIL) simulation to verify the results. The SOS method offers a more precise and less conservative representation of the stability region. Through applying the SOS method, this paper endeavors to establish and investigate the stability region for grid-tied IBR while conducting sensitivity analysis of the inverter responses to grid-side disturbances. This sensitivity analysis specifically delves into the impacts of different load levels and different voltage-loop control parameters on the stability region of the IBR and inverter transit response. In other words, the study develops a theoretical approach using the nonlinear dynamic model and Lyapunov-based stability assessment to understand how a modification in the system can affect the stability region of the IBR and the dynamic response of the inverter for a grid-side fault. The SOS method is applied to construct an accurate Lyapunov function for the system, and the Lyapunov-based stability assessment is used to study system stability under a large disturbance. Besides the numerical sensitivity analysis of inverter dynamic response, the accuracy of the sensitivity analysis is validated through complementary techniques, including time-domain simulations of a grid-tied IBR and high-fidelity HIL simulations using a real-time digital simulation (RTDS) platform. The result proves the outcomes of numerical stability analysis and sensitivity assessment of the IBR using an SOS-based stability analysis.

1. Introduction

1.1. Motivation and background

The primary driving force behind the development and implementation of inverter-based resources (IBRs) is the pursuit of reinforcing power supply resilience, dependability, and flexibility [1–3]. The utilization of IBR offers the potential for reducing operational costs and facilitating the effective integration of renewable energy sources [4,5]. Nevertheless, the application of IBRs, characterized by their low inertia, poses stability challenges and complexity, resulting in disconnecting IBRs due to grid disturbances. To effectively harness IBRs as reliable and flexible energy systems that enhance power supply resilience, stability assessment becomes a critical aspect, particularly for low-inertia IBRs. A comprehensive stability assessment can yield additional insights into the sensitivity of IBRs during transient faults and determine the maximum allowable duration for which an IBR can operate within a system without causing operational instability.

In the realm of system stability analysis, it is generally recognized that the classification can be based on the magnitude of the disturbance encountered, whether it is small or large [6]. For assessing small-signal stability, the use of linearization techniques and eigenvalue analysis proves useful in simplifying the system and stability analysis, respectively [7–9]. This approach yields results and analysis that specifically pertain to small transient disruptions [9,10], making it reliable for minor disturbances and contingencies such as load changes. However, its results are not authentic when addressing substantial disruptions

* Corresponding author.
E-mail addresses: hossei13@msu.edu (H. Hosseinpour), benidris@msu.edu (M. Ben-Idris).

https://doi.org/10.1016/j.epsr.2024.111020
Received 22 December 2023; Received in revised form 20 August 2024; Accepted 24 August 2024
Available online 7 September 2024

such as faults or line disconnections. Consequently, a large-signal stability assessment becomes necessary in order to obtain comprehensive information about the system's stability under both small and large disturbances.

1.2. Literature review and research gaps

The assessment of large-signal stability for IBRs has shown promise with the utilization of the Lyapunov-based technique [11–14], such that, in [13], a controller is proposed that can provide improved large-signal stability by enlarging the stability region, and in [15], large-stability analysis of a multi microgrid systems considering the communication delay time has been studied. This approach proves effective in accurately determining the stability boundary for nonlinear systems [16,17]. However, when it comes to inverter-based resources, which consist of a substantial number of nonlinear components, precise analysis of large-signal stability requires detailed models [18–20]. Applying methods based on Lyapunov theory, particularly those involving detailed models of components, has been notably difficult in evaluating the stability of power systems [12].

In analyzing and studying the stability and control of singular components such as converters, direct methods have been prominently utilized [16,21–24]. Different fault locations and types of systems integrated with IBRs are studied in [25,26], respectively. In [23], the large-signal stability analysis for a DC microgrid cluster has been studied using the Takagi–Sugeno method. A system-level large-signal stability for a droop-controlled DC inverter-based microgrid has been studied in [27] for constant load and for different types of load in [28]. Comprehensive large-signal stability analysis of a DC power system, including a singular inverter-based motor drive, is detailed in [29]. [30] offers an in-depth exploration of the stability sensitivity of an inverter-based microgrid with three inverter-based resources during various events by applying Krasovskii's methodological approach. Further, the large-signal stability of an inverter-based generator is examined in [31] using a Popov-driven Lyapunov function. Yet, it is important to note that the domain of attraction (DOA) delineated by the Popov-inspired direct method [32,33] tends to be conservative. Similarly, other techniques, like those built on Krasovskii's method [34], can also exhibit this conservative attribute [16].

In distribution systems and inverter-based resources, the constrained DOA, stemming from the adoption of conservative methodologies, predisposes the protection system to become overly protective in response to potential faults and contingencies. This often culminates in premature activation of the protection mechanisms [35,36]. The consequent unwarranted outages can lead to disruptions in supply, causing inconvenience for consumers. To address this conservativeness, the sum of squares method, as outlined in [37], presents a promising alternative for the stability assessment of any system. It offers a larger, verifiable DOA relative to traditional approaches like Popov [32,33] and Krasovskii's methods [34].

Generally, the stability region and critical stability boundary of a system after a modification or permanent change in the system, depending on the system configuration, current load and generation level, as well as current controlling setups, can improve or impair the DOA and system stability capability. In other words, examining the system stability region plays a pivotal role in comprehending the DOA behavior and assessing the system's stability capacity in response to various modifications. Such analysis yields valuable insights for enhancing the system's performance in the face of significant disturbances, such as faults.

In the context of a grid-connected IBR, it is frequently observed that these resources disconnect in response to grid-side disturbances as a proactive measure to safeguard system stability [25], such as in California in 2022 as NERC reported. However, this disconnection may not align with the original intent of the IBR application, which aimed to enhance both system reliability and stability.

1.3. Technical contributions

In this paper, the behavior of AC inverter-based resources during large disturbances is studied to analyze the sensitivity of the inverter during grid-side disturbances. Moreover, a sensitivity analysis for the stability region of inverter-based resources is developed by applying different permanent changes and modifications in the system. Also, the possibility of stability region improvement to keep IBRs connected to the grid during the grid-side large disturbance is scrutinized. The DOA in each case study is constructed for a nonlinear dynamic model of IBRs based on the SOS model, and the numerical analysis is verified using a real-time digital simulator (RTDS) for the sensitivity analysis of large-signal stability during large disturbances. The changes in the stability region under different modifications in the network are predicted based on the mathematical analysis and grid dynamic model, and the numerical analysis results are proved through RTDS and hardware-in-loop (HIL) testing. In this study:

- Formulated a detailed dynamic representation for an inverter-based resource, applying the sum of squares approach for the creation of the Lyapunov function.
- The sensitivity analysis of the stability region, as formulated through the sum of squares methods, is examined comparatively under two scenarios: the transient response of the system under a three-phase-to-ground fault for different load levels and under different control settings of the inverter.
- The accuracy of the result is validated through time-domain simulations and high-fidelity Hardware-in-the-loop (HIL) testing using real-time digital simulation (RTDS) systems.

The remainder of this paper is organized in the following manner. In Section 2, the nonlinear dynamic model and stability method are developed. Sections Section 4 studies numerical analysis results. Section 5 represents the HIL result and proof of the numerical analysis. Section 6 Concludes remarks.

2. Dynamic model of a grid-tied inverter-based resource

The meticulous dynamic modeling of Inverter-Based Resources and their controlling system are of paramount importance for the assessment of large-signal stability. This practice is instrumental in accurately forecasting system behavior under a spectrum of operational scenarios, particularly in the face of substantial disturbances. It underpins the assurance of system stability, a critical factor during pronounced perturbations. Furthermore, such modeling is integral to the sophisticated design and control of IBRs, facilitating the development of refined control strategies that ensure optimal functionality and stability. This aspect is especially vital for the harmonious integration of IBRs into the existing electrical grid infrastructure, mitigating the risk of system failures and enhancing overall grid resilience.

In Fig. 1, the network and control architecture of the inverter-based resource covered in this study are presented. This setup includes an inverter-based resource integrated with the main power grid and a connected load. The dynamic behavior of the inverter-based resource is encapsulated in a 13-order model, aligning with models described in Refs. [11,16,38]. Further sections will detail the theoretical underpinnings of this resource. The paper also models and demonstrates various components of the control system, such as power, voltage, and current control mechanisms, along with the RLC filter, line connections, and load interactions. Finally, a dynamic model for the IBR is developed by synthesizing all these components through an advanced network mapping strategy.

2.1. Power controller

The power controller assembly incorporates various elements such as the low-pass filter (ω_f), Q/V, and P/f configurations. A mathemat-

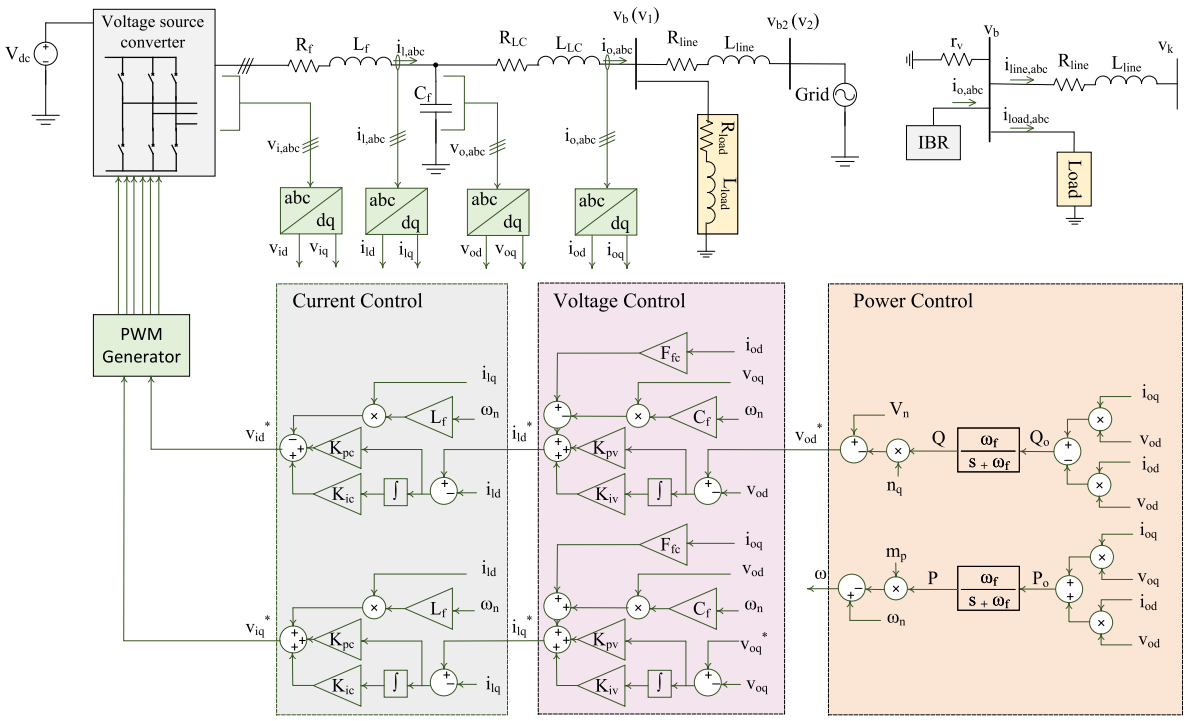

Fig. 1. A grid-tied inverter-based resource with the droop control system.

ically comprehensive description of the power controller's nonlinear dynamic model is provided in the subsequent section:

$$P = \frac{\omega_f}{s+\omega_f} P_o\,, \quad Q = \frac{\omega_f}{s+\omega_f} Q_o\,, \tag{1a}$$

$$P_o = i_{od}\, v_{od} + i_{oq}\, v_{oq}\,, \quad Q_o = -i_{oq}\, v_{od} + i_{od}\, v_{oq}, \tag{1b}$$

where i_{odq} and v_{odq} are the current and voltage at inverter output shown in Fig. 1. ω_f is equal to $2\pi f_f$, such that f_f shows the low-pass filter frequency

$$P = (\omega_n - \omega)/m_p\,, \quad Q = (V_n - v_{od}^*)/n_q\,, \quad v_{oq}^* = 0, \tag{2a}$$

$$\delta_n = \int (\omega - \omega_{\mathbf{m}}), \quad \Delta\,\omega_n = \omega_n - \omega_{\mathbf{m}}, \tag{2b}$$

where V_n and ω_n are the nominal voltage and frequency sets for the inverter control system. According to (1) and (2), the nonlinear dynamic model of the power controller is as follows:

$$\begin{aligned} \dot{X}_{P_{d,cntrl}} &= \mathbf{A_P}\, X_{P_{d,cntrl}} + \mathbf{B_{P1}}\, \Delta\,\omega_n + \mathbf{B_{P2}}\, U_{invr}, \\ Y_{P_{d,cntrl}} &= \mathbf{C_P}\, X_{P_{d,cntrl}} + \mathbf{E_P}, \end{aligned} \tag{3}$$

where

$$X^T_{P_{d,cntrl}} = \begin{bmatrix} \delta_n & P & Q \end{bmatrix}, \tag{4a}$$

$$Y^T_{P_{d,cntrl}} = \begin{bmatrix} \omega & v_{od}^* & v_{oq}^* \end{bmatrix}, \tag{4b}$$

$$U^T_{invr} = \begin{bmatrix} i_{ld} & i_{lq} & v_{od} & v_{oq} & i_{od} & i_{oq} \end{bmatrix}, \tag{4c}$$

$$\mathbf{A_P} = \begin{bmatrix} & -m_p & 0 \\ 0_{3\times1} & -\omega_f & 0 \\ & 0 & -\omega_f \end{bmatrix}, \ \mathbf{B_{P1}} = \begin{bmatrix} 1 \\ 0 \\ 0 \end{bmatrix}, \tag{4d}$$

$$\mathbf{B_{P2}} = \begin{bmatrix} & 0 & 0 \\ 0_{3\times4} & \omega_f\, v_{od} & \omega_f\, v_{oq} \\ & -\omega_f\, v_{oq} & \omega_f\, v_{od} \end{bmatrix}, \tag{4e}$$

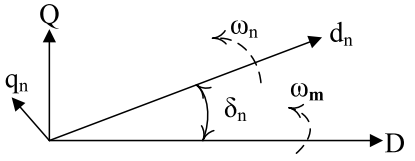

Fig. 2. Global $D-Q$ and local d-q reference frames.

$$\mathbf{C_P} = \begin{bmatrix} & -m_p & 0 \\ 0_{3\times1} & 0 & -n_q \\ & 0 & 0 \end{bmatrix}, \mathbf{E_P} = \begin{bmatrix} \omega_n \\ V_n \\ 0 \end{bmatrix}, \tag{4f}$$

where $\omega_{\mathbf{m}}$, and ω are the angular frequencies for global and local rotating reference frames, respectively. The angle between the global reference and the inverter's local frames is δ (illustrated in Fig. 2).

2.2. Voltage controller

In the droop control of an inverter, the voltage control loop is essential for maintaining the stability and quality of the power supply. The voltage control loop in droop control regulates the output voltage of the inverter to ensure it is at the desired level despite load changes or other disturbances. The dynamic of the voltage control loop in the context of droop control can be described as follows:

$$\frac{\mathrm{d}\mathcal{V}_d}{\mathrm{d}t} = v_{od}^* - v_{od}, \quad \frac{\mathrm{d}\mathcal{V}_q}{\mathrm{d}t} = v_{oq}^* - v_{oq}, \tag{5}$$

where the voltage deviation from the reference voltage value is defined by $\mathcal{V}$. The dynamic of the voltage control loop can be modified to a matrix-based dynamic model as follows:

$$\begin{aligned} \dot{X}_{\mathcal{V}_{d,cntrl}} &= \mathbf{A_v}\, X_{\mathcal{V}_{d,cntrl}} + \mathbf{B_{v1}}\, U_v + \mathbf{B_{v2}}\, U_{invr}, \\ Y_{\mathcal{V}_{d,cntrl}} &= \mathbf{C_v}\ X_{\mathcal{V}_{d,cntrl}} + \mathbf{D_{v1}}\, U_v + \mathbf{D_{v2}}\, U_{invr}, \end{aligned} \tag{6}$$

where

$$X_{\mathcal{V}_{d,cntrl}} = \begin{bmatrix} \mathcal{V}_d \\ \mathcal{V}_q \end{bmatrix}, \ Y_{\mathcal{V}_{d,cntrl}} = \begin{bmatrix} i_{ld}^* \\ i_{lq}^* \end{bmatrix}, \tag{7a}$$

$$U_v = \begin{bmatrix} v^*_{od} \\ v^*_{oq} \end{bmatrix}, \ \mathbf{A_v} = \begin{bmatrix} 0 & 0 \\ 0 & 0 \end{bmatrix}, \tag{7b}$$

$$\mathbf{B_{v1}} = \begin{bmatrix} 1 & 0 \\ 0 & 1 \end{bmatrix}, \mathbf{B_{v2}} = \begin{bmatrix} 0 & 0 & -1 & 0 & 0 & 0 \\ 0 & 0 & 0 & -1 & 0 & 0 \end{bmatrix}, \tag{7c}$$

$$\mathbf{C_v} = \begin{bmatrix} \mathcal{K}_{iv} & 0 \\ 0 & \mathcal{K}_{iv} \end{bmatrix}, \mathbf{D_{v1}} = \begin{bmatrix} \mathcal{K}_{pv} & 0 \\ 0 & \mathcal{K}_{pv} \end{bmatrix}, \tag{7d}$$

$$\mathbf{D_{v2}} = \begin{bmatrix} 0 & 0 & -\mathcal{K}_{pv} & -\omega_n C_f & \mathcal{F}_{fc} & 0 \\ 0 & 0 & \omega_n C_f & -\mathcal{K}_{pv} & 0 & \mathcal{F}_{fc} \end{bmatrix}, \tag{7e}$$

where $\mathcal{F}_{fc}$, $(.)_{iv}$, and $(.)_{pv}$ denote the feed-forward coefficient, the integral (I) coefficient, and the proportional (P) coefficient of the inverter's voltage controller, respectively.

2.3. Current controller

In the droop control of inverters, alongside the voltage control loop, the current control loop plays a pivotal role in maintaining the stability and quality of the power output. It helps to regulate the output current to ensure it remains at the desired level, catering for changes in load and other disturbances effectively. The matrix-based dynamic model of the current controller is formulated as follows:

$$\frac{\mathrm{d}\mathcal{I}_d}{\mathrm{d}t} = i^*_{ld} - i_{ld}, \quad \frac{\mathrm{d}\mathcal{I}_q}{\mathrm{d}t} = i^*_{lq} - i_{lq}, \tag{8}$$

where $\mathcal{I}$ is defined as the deviation of current observed in the local d-q reference frame from nominal values. Subsequent to this definition, the construction of the matrix-based dynamic model associated with the current controller loop is methodically delineated:

$$\begin{aligned} \dot{X}_{\mathcal{I}_{d,cntrl}} &= \mathbf{A_c}\, X_{\mathcal{I}_{d,cntrl}} + \mathbf{B_{c1}}\, U_c + \mathbf{B_{c2}}\, U_{invr}, \\ Y_{\mathcal{I}_{d,cntrl}} &= \mathbf{C_c}\ X_{\mathcal{I}_{d,cntrl}} + \mathbf{D_{c1}}\, U_c + \mathbf{D_{c2}}\, U_{invr}, \end{aligned} \tag{9}$$

where

$$X_{\mathcal{I}_{d,cntrl}} = \begin{bmatrix} \mathcal{I}_d \\ \mathcal{I}_q \end{bmatrix}, U_c = \begin{bmatrix} i^*_{ld} \\ i^*_{lq} \end{bmatrix}, Y_{\mathcal{I}_{d,cntrl}} = \begin{bmatrix} v^*_{id} \\ v^*_{iq} \end{bmatrix}, \tag{10a}$$

$$\mathbf{A_c} = \begin{bmatrix} 0 & 0 \\ 0 & 0 \end{bmatrix}, \mathbf{B_{c1}} = \begin{bmatrix} 1 & 0 \\ 0 & 1 \end{bmatrix}, \tag{10b}$$

$$\mathbf{B_{c2}} = \begin{bmatrix} -1 & 0 & 0_{1\times4} \\ 0 & -1 & 0_{1\times4} \end{bmatrix}, \mathbf{C_c} = \begin{bmatrix} \mathcal{K}_{ic} & 0 \\ 0 & \mathcal{K}_{ic} \end{bmatrix}, \tag{10c}$$

$$\mathbf{D_{c1}} = \begin{bmatrix} \mathcal{K}_{pc} & 0 \\ 0 & \mathcal{K}_{pc} \end{bmatrix}, \mathbf{D_{c2}} = \begin{bmatrix} -\mathcal{K}_{pc} & -\omega_n L_f & 0_{1\times4} \\ \omega_n L_f & -\mathcal{K}_{pc} & 0_{1\times4} \end{bmatrix}. \tag{10d}$$

where the proportional–integral (PI) coefficients assigned to the current controller are denoted as $\mathcal{K}_{ic}$ for the integral component and $\mathcal{K}_{pc}$ for the proportional component.

2.4. RLC filter

The RLC filter in droop control of an inverter is crucial for attenuating switching harmonics and improving the quality of the inverter's output voltage and current. RLC filters consist of three resistors (R), inductors (L), and a capacitor (C), and they are helpful in suppressing the higher frequency harmonics generated by the inverter's switching actions. the dynamic of the RLC filter circuit is formulated as follows:

$$\frac{\mathrm{d}i_{ld}}{\mathrm{d}t} = \frac{1}{L_f}(v_{id} - v_{od}) + \omega\, i_{lq} - \frac{r_f}{L_f} i_{ld}, \tag{11a}$$

$$\frac{\mathrm{d}i_{lq}}{\mathrm{d}t} = \frac{1}{L_f}(v_{iq} - v_{oq}) - \omega\, i_{ld} - \frac{r_f}{L_f} i_{lq}, \tag{11b}$$

$$\frac{\mathrm{d}i_{od}}{\mathrm{d}t} = \frac{1}{L_c}(v_{od} - v_{bd}) + \omega\, i_{oq} - \frac{r_c}{L_c} i_{od}, \tag{11c}$$

$$\frac{\mathrm{d}i_{oq}}{\mathrm{d}t} = \frac{1}{L_c}(v_{oq} - v_{bq}) - \omega\, i_{od} - \frac{r_c}{L_c} i_{oq}, \tag{11d}$$

$$\frac{\mathrm{d}v_{od}}{\mathrm{d}t} = \frac{1}{C_f}(i_{ld} - i_{od}) + \omega\, v_{oq}, \tag{11e}$$

$$\frac{\mathrm{d}v_{oq}}{\mathrm{d}t} = \frac{1}{C_f}(i_{lq} - i_{oq}) - \omega\, v_{od}. \tag{11f}$$

The RLC filter's dynamic model can be articulated in the following manner:

$$\dot{X}_{LC_{fltr}} = \mathbf{A_{LC}}\, X_{LC_{fltr}} + \mathbf{B_{LC1}}\, U_{LC1} + \mathbf{B_{LC2}}\, U_{LC2}, \tag{12}$$

where

$$X_{LC_{fltr}} = U_{invr}, \tag{13a}$$

$$U_{LC1} = \begin{bmatrix} v_{id} \\ v_{iq} \end{bmatrix}, U_{LC2} = \begin{bmatrix} v_{bd} \\ v_{bq} \end{bmatrix}. \tag{13b}$$

$$\mathbf{A_{LC}} = \begin{bmatrix} \frac{-r_f}{L_f} & \omega_{\mathbf{m}} & \frac{-1}{L_f} & 0 & 0 & 0 \\ -\omega_{\mathbf{m}} & \frac{-r_f}{L_f} & 0 & \frac{-1}{L_f} & 0 & 0 \\ \frac{1}{C_f} & 0 & 0 & \omega_{\mathbf{m}} & \frac{-1}{C_f} & 0 \\ 0 & \frac{1}{C_f} & -\omega_{\mathbf{m}} & 0 & 0 & \frac{-1}{C_f} \\ 0 & 0 & \frac{1}{L_c} & 0 & \frac{-r_c}{L_c} & \omega_{\mathbf{m}} \\ 0 & 0 & 0 & \frac{1}{L_c} & -\omega_{\mathbf{m}} & \frac{-r_c}{L_c} \end{bmatrix}, \tag{13c}$$

$$\mathbf{B_{LC1}} = \begin{bmatrix} \frac{1}{L_f} & 0 \\ 0 & \frac{1}{L_f} \\ 0_{4\times2} & \end{bmatrix}, \mathbf{B_{LC2}} = \begin{bmatrix} 0_{4\times2} & \\ \frac{-1}{L_c} & 0 \\ 0 & \frac{-1}{L_c} \end{bmatrix}, \tag{13d}$$

where v_{bd} and v_{bq} are the output voltages shown in Fig. 1.

2.5. Dynamic model of the inverter-based resource

The system is considered balanced and is free from harmonic distortions. Consequently, the integrated matrix-based dynamic model for an inverter-based resource is articulated as follows:

$$\begin{aligned} \dot{X}_{IBR} &= \mathbf{A_{IBR}}\, X_{IBR} + \mathbf{B_{IBR1}}\, U_{IBR} + \mathbf{B_{IBR2}} + \mathbf{B_{IBR3}}\, \omega_{\mathbf{m}}, \\ Y_{IBR} &= \mathbf{C_{IBR}}\, X_{IBR} + \mathbf{D_{IBR1}}\, \omega_n, \end{aligned} \tag{14}$$

where (see the Eq. (16) in Box I)

$$X^T_{IBR} = [\delta \quad P \quad Q \quad \mathcal{V}_d \quad \mathcal{V}_q \quad \mathcal{I}_d \quad \mathcal{I}_q \quad i_{ld} \quad i_{lq} \quad v_{od} \quad v_{oq} \quad i_{od} \quad i_{oq}], \tag{15a}$$

$$U^T_{IBR} = [v_{bD} \quad v_{bQ}], \ Y^T_{IBR} = [\omega_n \quad i_{oD} \quad i_{oQ}], \tag{15b}$$

$$\mathbf{B^T_{IBR1}} = \frac{-1}{L_c}\begin{bmatrix} 0_{1\times11} & \cos(\delta) & -\sin(\delta) \\ 0_{1\times11} & \sin(\delta) & \cos(\delta) \end{bmatrix}, \tag{15c}$$

$$\mathbf{B^T_{IBR2}} = [\omega_n \quad 0_{1\times2} \quad V_n \quad 0 \quad (\mathcal{K}_{pv}V_n) \quad 0_{1\times7}], \tag{15d}$$

$$\mathbf{B^T_{IBR3}} = [-1 \quad 0_{1\times12}], \mathbf{D^T_{IBR}} = [1 \quad 0_{1\times2}], \tag{15e}$$

$$\mathbf{C^T_{IBR}} = \begin{bmatrix} 0 & 0 \\ 0_{3\times11} & \cos(\delta) & -\sin(\delta) \\ & \sin(\delta) & \cos(\delta) \end{bmatrix}, \mathbf{C'^T_P} = \begin{bmatrix} 0_{2\times1} \\ -n_q \end{bmatrix}. \tag{15f}$$

$$\mathbf{A_{IBR}} = \begin{bmatrix} \mathbf{A_P} & 0_{3\times4} & \mathbf{B_P} & \\ \mathbf{B_{v1}}\,\mathbf{C'_P} & 0_{2\times4} & \mathbf{B_{v2}} & \\ \mathbf{B_{c1}}\,\mathbf{D_{v1}}\,\mathbf{C'_P} & \mathbf{B_{c1}}\,\mathbf{C_v} & 0_{2\times2} & \mathbf{B_{c1}}\,\mathbf{D_{v2}} + \mathbf{B_{c2}} \\ \zeta\,\mathbf{B_{LC1}}\,\mathbf{D_{c1}}\,\mathbf{D_{v1}}\,\mathbf{C'_P} & \zeta\,\mathbf{B_{LC1}}\,\mathbf{D_{c1}}\,\mathbf{C_v} & \zeta\,\mathbf{B_{LC1}}\,\mathbf{C_c} & \gamma \end{bmatrix}_{13\times13}, \tag{16}$$

$$\zeta = \mathcal{G}_{IBR}\,V_{dc}\,,\quad \gamma = \mathbf{A_{LC}} + \zeta\,\mathbf{B_{LC1}}\,(\mathbf{D_{c1}}\,\mathbf{D_{v2}} + \mathbf{D_{c2}})\,,\quad \mathbf{C'_P}^{\mathbf{T}} = \begin{bmatrix} 0_{2\times1} \\ -n_q \end{bmatrix}.$$

Box I.

2.6. Network

By considering the network and lines, the nonlinear dynamic model of the system can be modified and reformulated as follows:

$$\frac{\mathrm{d}i_{line,D}}{\mathrm{d}t} = -\frac{(v_{kD} - v_{bD} + r_{line}\,i_{line,D})}{L_{line}} + \omega\,i_{line,Q}, \tag{17a}$$

$$\frac{\mathrm{d}i_{line,Q}}{\mathrm{d}t} = -\frac{(v_{kQ} - v_{bQ} + r_{line}\,i_{line,Q})}{L_{line}} - \omega\,i_{line,D}, \tag{17b}$$

where

$$\dot{X}_{i_{grid}} = \mathbf{A_{grid}}\,X_{i_{grid}} + \mathbf{B_{grid}}\,U_{grid}, \tag{18}$$

$$X_{i_{grid}} = \left[X_{i_{line}}\right],\ U_{grid} = \begin{bmatrix} v_{bDQ1} \\ v_{bDQ2} \end{bmatrix}, \tag{19a}$$

$$X_{i_{line}} = \begin{bmatrix} i_{line,D} \\ i_{line,Q} \end{bmatrix},\quad v_{bDQ} = \begin{bmatrix} v_{bD} \\ v_{bQ} \end{bmatrix}, \tag{19b}$$

$$\mathbf{A_{grid}} = \left[\mathbf{A_{line}}\right],\quad \mathbf{B_{grid}} = \left[\mathbf{B_{line}}\right], \tag{19c}$$

$$\mathbf{A_{line}} = \begin{bmatrix} -r_{line}/L_{line} & \omega_{\mathbf{m}} \\ -\omega_{\mathbf{m}} & -r_{line}/L_{line} \end{bmatrix}, \tag{19d}$$

$$\mathbf{B_{line}} = \begin{bmatrix} \frac{1}{L_{line}} & 0 & \frac{-1}{L_{line}} & 0 \\ 0 & \frac{1}{L_{line}} & 0 & \frac{-1}{L_{line}} \end{bmatrix}. \tag{19e}$$

$\leftarrow node\ b \rightarrow$ $\leftarrow node\ k \rightarrow$

In this context, $(.)_{\mathbf{line}}$ is a symbol representing the lines' connectivity to the nodes. Additionally, as illustrated in Fig. 1, v_k and v_b correspond to v_{b2} (or v_2 as shown in Fig. 1) and v_{b1}, in that order. The line current in the $\mathbf{B_{grid}}$ matrix flows outward from node b (indicated as $+1/L_{line}$) and inward towards node k (notated as $-1/L_{line}$). All remaining entries in the $\mathbf{B_{grid}}$ matrix are assigned a value of zero.

2.7. Load model

The load model characterizes the dynamic response of loads in the system, accounting for variations in voltage and frequency. It encompasses a range of parameters, such as resistive, inductive, and capacitive components, to accurately represent load behavior under various conditions. In this study, a common sort of constant resistive-inductive (RL) load is considered as the load model that its circuit is formulated as follows:

$$\frac{\mathrm{d}i_{load,D}}{\mathrm{d}t} = \frac{-R_{load}\,i_{load,D}}{L_{load}} + \frac{v_{bD}}{L_{load}} + \omega\,i_{load,Q}, \tag{20a}$$

$$\frac{\mathrm{d}i_{load,Q}}{\mathrm{d}t} = \frac{-R_{load}\,i_{load,Q}}{L_{load}} + \frac{v_{bQ}}{L_{load}} - \omega\,i_{load,D}. \tag{20b}$$

For the dynamic model of the load, the following model is developed:

$$\dot{X}_{i_{load}} = \mathbf{A_{load}}\,X_{i_{load}} + \mathbf{B_{load}}\,U_{load}, \tag{21}$$

where

$$X_{i_{load}} = \begin{bmatrix} i_{load,D} \\ i_{load,Q} \end{bmatrix},\ U_{load} = U_{LC2}\,[T_{DQ}] = \begin{bmatrix} v_{bD} \\ v_{bQ} \end{bmatrix}, \tag{22a}$$

$$\mathbf{A_{load}} = \begin{bmatrix} -R_{load}/L_{load} & \omega_{\mathbf{m}} \\ -\omega_{\mathbf{m}} & -R_{load}/L_{load} \end{bmatrix}, \tag{22b}$$

$$\mathbf{B_{load}} = \begin{bmatrix} 1/L_{load} & 0 \\ 0 & 1/L_{load} \end{bmatrix}. \tag{22c}$$

The local $d-q$ parameter can be transferred to the global reference using T_{DQ}.

2.8. Grid mapping

In the quest to ascertain the voltage at individual nodes within the microgrid, a strategic approach involves the insertion of a virtual resistor, denoted as r_v, between each node and the ground as depicted in Fig. 1. The critical consideration here is the selection of a substantially high value for r_v in order to effectively mitigate any possible detrimental influences on the precision of the dynamic model. Consequently, the node voltage can be precisely determined through the utilization of the ensuing equation:

$$v_{bDQ} = \mathbf{R_v}(\mathbf{M_{IBR}}i_{oDQ} + \mathbf{M_L}i_{loadDQ} + \mathbf{M_{grid}}i_{lineDQ}), \tag{23}$$

where **L**, **grid**, and **IBR** denote subscripts for load, line, and inverter models, respectively. Within the $\mathbf{R_v}$ matrix, the diagonal elements are set to r_v. The $\mathbf{M_{IBR}}$ matrix encompasses the connections between inverters and nodes, with a value of 1 at row i and column j if inverter j is connected to node i, and 0 otherwise. $\mathbf{M_L}$ maps the relationships between loads and nodes, with an element at row i and column j being 1 when there is a connection between node i and load j and 0 otherwise. Meanwhile, the $\mathbf{M_{grid}}$ matrix describes the direction of current flow in each line, with a value of 1 at row i and column j if the current of line j is injected into node i and -1 otherwise [11,38]. Consequently, the grid-tied IBR depicted in Fig. 1 can be presented using a matrix-based dynamic model as follows:

$$\dot{X}_{\mathbf{G-IBR}} = \mathbf{A_{G-IBR}}\,X_{\mathbf{G-IBR}} + \mathbf{B_{G-IBR}}, \tag{24}$$

where

$$\mathbf{B_{IBR}} = \mathbf{B_{IBR2}} + \mathbf{B_{IBR3}}\,\omega_{\mathbf{m}}, \tag{25a}$$

$$X_{\mathbf{G-IBR}} = \begin{bmatrix} X_{\mathbf{IBR}} \\ i_{line,DQ} \\ i_{load,DQ} \end{bmatrix},\ \mathbf{B_{G-IBR}} = \begin{bmatrix} \mathbf{B_{IBR}} \\ 0_{2\times1} \\ 0_{2\times1} \end{bmatrix}. \tag{25b}$$

$$\mathbf{A_{G-IBR}} = \begin{bmatrix} \mathbf{A_{IBR}} + \mathbf{B_{IBR}}\mathbf{R_v}\mathbf{M_{IBR}}\mathbf{C_{IBR_c}} & \mathbf{B_{IBR}}\mathbf{R_v}\mathbf{M_{grid}} & \mathbf{B_{IBR}}\mathbf{R_v}\mathbf{M_L} \\ \mathbf{B_{grid}}\mathbf{R_v}\mathbf{M_{IBR}}\mathbf{C_{IBR_c}} & \mathbf{A_{grid}} + \mathbf{B_{grid}}\mathbf{R_v}\mathbf{M_{grid}} & \mathbf{B_{grid}}\mathbf{R_v}\mathbf{M_L} \\ \mathbf{B_{load}}\mathbf{R_v}\mathbf{M_{IBR}}\mathbf{C_{IBR_c}} & \mathbf{B_{load}}\mathbf{R_v}\mathbf{M_{grid}} & \mathbf{A_{load}} + \mathbf{B_{load}}\mathbf{R_v}\mathbf{M_L} \end{bmatrix}. \tag{26}$$

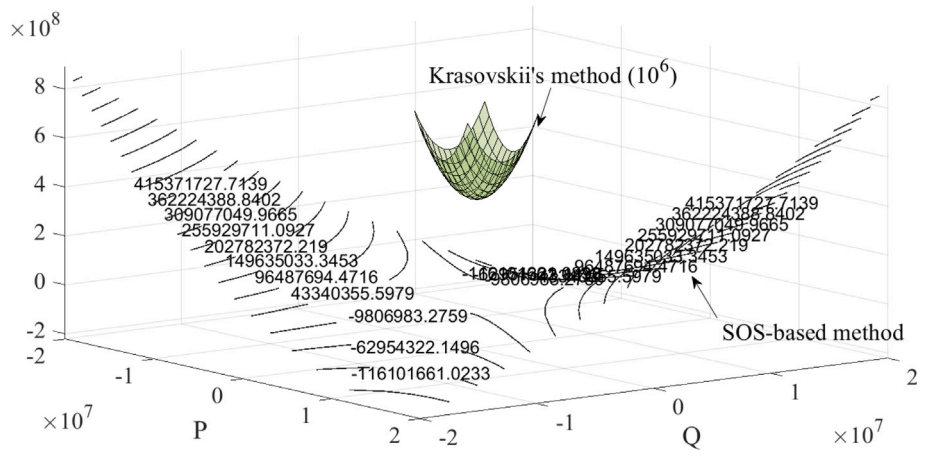

Fig. 3. Stability region for Krasovskii's (green surf) and SOS-based (contour) methods.

3. Constructing the Lyapunov function

The Lyapunov function that has been formulated must satisfy the following conditions to establish the stability region in accordance with Lyapunov-based stability analysis:

$$\begin{cases} \text{For } \mathbf{X^n_{G-IBR}} = 0, \text{ the } \mathcal{V}_L \text{ value is equal to zero. } \Rightarrow \mathcal{V}_L(0) = 0 \\ \text{The defined } \mathcal{V}_L \text{ is positive inside the stability region.} \\ \quad \Rightarrow \mathcal{V}_L(\mathbf{X^n_{G-IBR}}) > 0 \\ \text{The defined } \dot{\mathcal{V}}_L \text{ indicate a downward slope in stability region.} \\ \quad \Rightarrow \dot{\mathcal{V}}_L(\mathbf{X^n_{G-IBR}}) \leq 0 \end{cases} \tag{27}$$

For the initial condition, the network's dynamic model is transitioned to its steady-state operating or equilibrium point. In this context, the steady-state operating point is defined as an operating point that has the minimum energy level or $\mathcal{V}_L$ value; in other words, $\mathbf{X^{con}_{G-IBR}} = \mathbf{X_{G-IBR}} - \mathbf{X^{eq}_{G-IBR}}$, such that $\dot{\mathbf{X}}^{\mathbf{con}}_{\mathbf{G-IBR}} = \mathbf{A_{G-IBR}}(\mathbf{X^{con}_{G-IBR}})\mathbf{X^{con}_{G-IBR}}$. $\mathbf{X^{eq}_{G-IBR}}$ is the equilibrium point of the system. Thus, $\mathcal{V}_L(\mathbf{X^{con}_{G-IBR}})$ is 0 for $\mathbf{X^{con}_{G-IBR}} = 0$.

Parrilo's seminal work introduced the sum of squares (SOS) method, a groundbreaking approach that has since been instrumental in addressing a myriad of complex problems in system analysis [39]. This innovative technique has particularly been influential in overcoming previously insurmountable challenges associated with the systematic, mathematical stability analysis of a system, employing advanced Lyapunov methodologies.

In the realm of nonlinear dynamics and control, the SOS-based stability method has garnered recognition for its precision and robustness in analyzing the stability of complex systems [40,41]. Mathematically, this approach is rooted in the optimization of polynomial Lyapunov functions and the delineation of regions of attraction, facilitating a comprehensive stability assessment. The general step for Lyapunov-based stability analysis is described as follows [42]:

- Consider a nonlinear dynamical system represented as

$$\dot{\mathbf{X}} = f(\mathbf{X}), \mathbf{X} \in \mathcal{R}, \tag{28}$$

where $\mathbf{X}$ is the state vector and $f : \mathbb{R}^n \to \mathbb{R}^n$ is a continuously differentiable vector field. The objective is to ascertain the stability of the equilibrium point $\mathbf{X} = 0$.

A polynomial Lyapunov function $\mathcal{V}_L(\mathbf{X})$ is employed, where $\mathcal{V}_L : \mathbb{R}^n \to \mathbb{R}^n$, satisfying the following conditions:

$$\begin{cases} \mathcal{V}_L(0) = 0, \\ \mathcal{V}_L(\mathbf{X}) > 0 \ , \forall \mathbf{X} \neq 0, \\ \dot{\mathcal{V}}_L(\mathbf{X}) = \nabla \mathcal{V}_L(\mathbf{X})^T f(\mathbf{X}) < 0 \ , \forall \mathbf{X} \neq 0. \end{cases} \tag{29}$$

The SOS-based stability method exploits sum of squares programming to verify these conditions. Specifically, $\mathcal{V}_L(\mathbf{X})$ and $-\dot{\mathcal{V}}_L(\mathbf{X})$ are expressed as SOS polynomials, ensuring their positivity and hence validating the stability criteria.

- A polynomial $p(\mathbf{X})$ of degree $2d$ is a sum of squares if there exist polynomials $q_i(\mathbf{X})$ such as follows:

$$p(\mathbf{X}) = \sum_{i=1}^{m} q_i^2(\mathbf{X}), \tag{30}$$

where $(\mathbf{X})$ is a vector of variables $\mathbf{X} = [\mathbf{X}_1, \mathbf{X}_2, \ldots, \mathbf{X}_n]^T$, m is the number of terms in the sum, and $q_i(\mathbf{X})$ are polynomials in $(\mathbf{X})$. Each $q_i(\mathbf{X})$ can be of varying degrees, and they are not necessarily unique or distinct from each other. $q_i^2(\mathbf{X})$ represents individual polynomial expressions. If d is considered the degree of the polynomials, in the context of an SOS, the polynomial $p(x)$ is represented as a sum of squares and typically has a degree of $2d$. This means that the highest power of any variable in the polynomial is $2d$. The key characteristic of a sum of squares polynomial is that each $q_i^2(\mathbf{X})$ term is always non-negative for any value of $(\mathbf{X})$, ensuring that $p(\mathbf{X})$ as a whole is non-negative.
- The stability of the equilibrium point is ascertained by constructing a Lyapunov function $\mathcal{V}_L(\mathbf{X})$ as an SOS polynomial and ensuring that $-\dot{\mathcal{V}}_L(\mathbf{X})$ is also an SOS, thus affirming the negative definiteness of $\dot{\mathcal{V}}_L(\mathbf{X})$. Using SOSTOOLS [43] or similar computational tools, $\mathcal{V}_L(\mathbf{X})$ and validate the conditions are as follows:

$$\begin{cases} \mathcal{V}_L(\mathbf{X}) - \epsilon \parallel \mathbf{X} \parallel^2 \quad \text{is SOS}, \\ -\dot{\mathcal{V}}_L(\mathbf{X}) - \epsilon \parallel \mathbf{X} \parallel^2 \quad \text{is SOS}, \end{cases} \quad \text{for some } \epsilon > 0, \tag{31}$$

where $\parallel \mathbf{X} \parallel^2$ is a norm square of the state vector $\mathbf{X}$.
- The region of attraction is delineated by the sub-level set

$$\mathcal{R} = \{\mathbf{X} \in \mathbb{R}^n : \mathcal{V}_L(\mathbf{X}) \leq \kappa\} \tag{32}$$

for some $\kappa > 0$. The boundary of $\mathcal{R}$, represented by the level set $\mathcal{V}_L(\mathbf{X}) = \kappa$, is computed as an SOS to ensure that the region of attraction is estimated with minimal conservativeness.

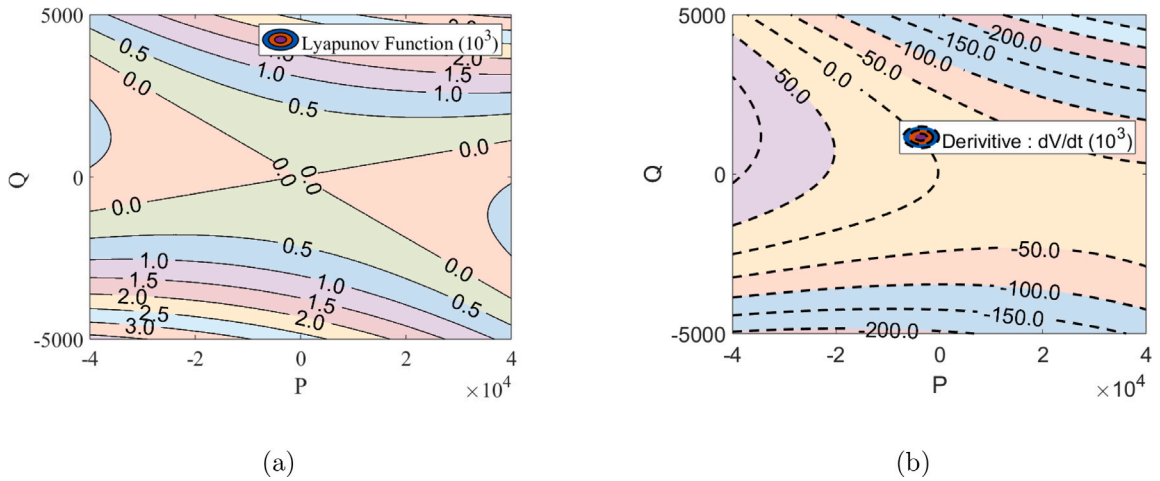

Fig. 4. Constructing Lyapunov function, $\mathcal{V}_L$, based on SOS model: (a) Lyapunov function and (b) derivative of Lyapunov function.

Table 1
The variables associated with the control of the inverter and the load.

Parameter	Value	Parameter	Value
V_n	381 V	w_f	12π rad/s
w_n	120π rad/s	$\omega_{\mathbf{m}}$	120π rad/s
m_p	9.35e−6	n_q	3.4e−5
$\mathcal{K}_{iv}$	405	$\mathcal{K}_{pv}$	0.51
$\mathcal{K}_{pc}$	10.5	$\mathcal{K}_{ic}$	12e4
$\mathcal{F}_{fc}$	0.73	r_N	8600 Ω
L_{grid}	5 mH	r_{grid}	34 Ω
L_{load}	0.5 mH	r_{load}	25 Ω
L_c	3.4 mH	r_c	0.052 Ω
L_f	13.6 mH	r_f	0.03 Ω
C_f	66 μF		

The SOS-based stability method, underpinned by rigorous mathematical formulations and computational techniques, provides a systematic and robust means to assess the stability of nonlinear dynamical systems. Its ability to optimize Lyapunov functions and delineate precise regions of attraction ensures comprehensive insights into system dynamics, fostering enhanced predictability and control.

4. Numerical analysis

The developed nonlinear dynamic model and the mentioned direct method for stability analysis, the SOS-based method, are applied to construct the stability region of an IBR with a load to analyze its stability against grid-side disturbances. The case study involves an inverter-based resource connected to the main grid and a load. The grid parameters are listed in Table 1. The transient response of the system under a transient three-phase-to-ground fault is scrutinized under two system conditions: different load levels and different control settings of the inverter.

4.1. Results and discussion

4.1.1. Comparison

Fig. 3 virtually represents that the technique in the SOS method possesses the capability to expand the operating stability region into a confirmable state space, reinforcing the precision assertions previously stated for the Lyapunov function constructed by the SOS-based model. A comparative analysis between the DOA formed utilizing two distinct approaches — Krasovskii's method [30,34,44] and the SOS-based technique is offered in Fig. 3 for the system tabulated in Table 1. This comparison underscores the enhanced efficacy and accuracy of the constructed stability region based on the SOS model, showcasing its potential to broaden the DOA effectively. The domain of attraction secured through Krasovskii's method is notably constrained when compared with the SOS-based approach. In the context of inverter stability, responses to contingencies under Krasovskii's protocol tend to be overly cautious, a consequence stemming from the confined DOA that this method delineates. The limited scope of attraction defined by Krasovskii's approach often results in a conservative response pattern, underscoring the comparative expansiveness and adaptability of the SOS-based technique.

Fig. 4 illustrates the Lyapunov function based on SOS model and its corresponding derivative. Fig. 4-(a) and (b) illustrate that the constructed Lyapunov unction by the SOS-based method can satisfy the second and third conditions of Lyapunov-based stability conditions. The following section delves into an analysis of the effects of load variations and control system adjustments on the stability region of the system.

4.1.2. Transient response to a fault for different load levels

Load reconfiguration serves as a pivotal strategy for enhancing system reliability during unforeseen events, instigating a modification in the stability region and system response during faults and other large disturbances. A well-executed load adjustment or diminution can expand this region, avoiding disconnecting the inverter from the grid due to grid-side disturbance and strengthening the network's resilience against transient faults. This strategic modulation of load optimizes the system's robustness against large disturbances, minimizing the possibility of disruptions or failures and elevating overall operational efficiency.

The transient response of the system to a three-phase-to-ground fault under two different load levels is represented in Fig. 5-(a). Increasing the load amount at node 1 results in the compression of contour lines for identical $\mathcal{V}_L$-slices towards a diminished stability region, signaling a decline in the system's stability threshold; in other words, to guarantee a stable transient response, the fault must be cleared sooner compared to the system with lower load level. In essence, augmented load constraints the system's stability region, escalating the probability of instability and potential operational failure under large disturbances like faults.

4.1.3. Voltage control coefficient, $\mathcal{K}_{pv}$

Inverter switching systems utilize a diverse array of control strategies to guarantee both stability and reliability in their operation. Engineered for adaptability, smart control systems are equipped to recalibrate control parameters during regular and emergency scenarios. The operational intelligence of these systems is anchored in a set of control objects that underpin decision-making processes for the switching systems.

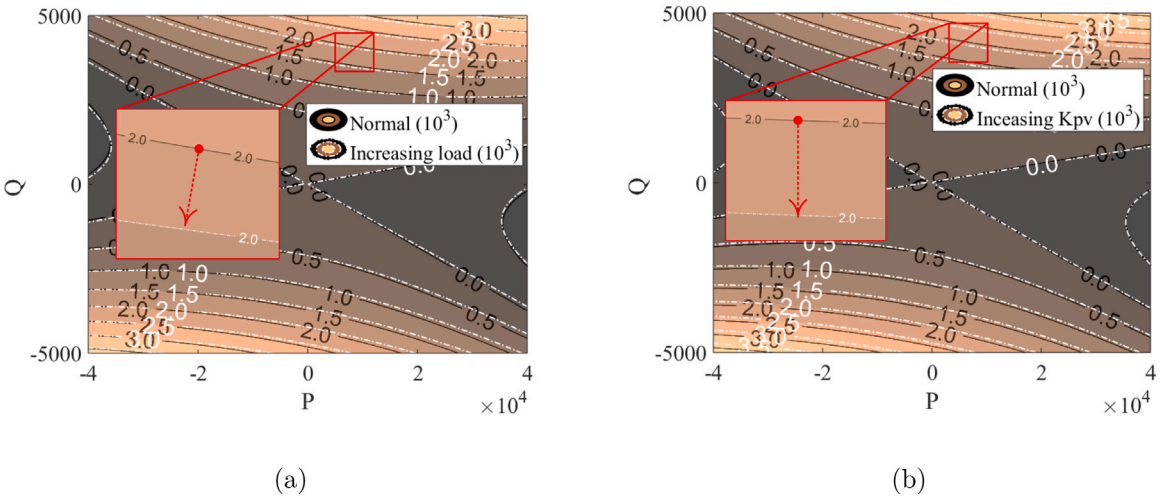

Fig. 5. Lyapunov function constructed using SOS-based model: (a) effect of change in load on DOA, and (b) effect of change in the voltage control system, $\mathcal{K}_{pv}$, on DOA.

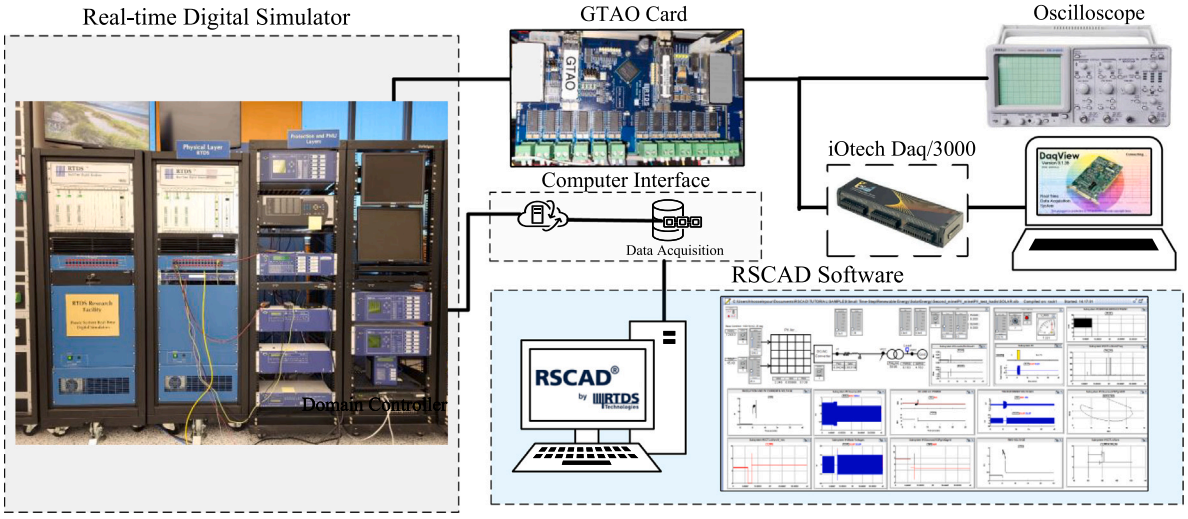

Fig. 6. The framework of the real-time digital simulator.

The region of attraction emerges as a supplementary benchmark in this context, offering an additional layer of criteria that influence the adjustment of control parameters. Consequently, the smart control system is attuned to respond adeptly to the dynamic shifts in system behavior. This responsiveness ensures that the inverter switching systems maintain stability and reliability even during fluctuating operational conditions.

As depicted in Fig. 5-(b), by increasing the voltage control loop parameter of the system, $\mathcal{K}_{pv}$, the contour lines representing equal values of the Lyapunov function in both case study are diminished in size. It means the operating point of the system will reach its critical stability energy boundary faster for the system with a large $\mathcal{K}_{pv}$ during the same fault. The numerical analysis can help to understand how any modification in the control system parameters affects the system stability region. Therefore, precision in tuning the control parameters is instrumental in elevating the robustness of the system, ensuring it is fortified against fluctuations and uncertainties as well as primed for optimal performance.

5. Assessment using real-time digital simulators

Real-time digital simulators (RTDS) provide an environment to simulate IBRs in real-time and enable HIL testing. RTDS can help simulate disturbance scenarios for a specific system and illustrate the possible challenges of the system under the disturbance. Theoretical analysis of system stability plays a crucial role in examining stability across multiple scenarios. Fig. 6 represents the real-time simulator setup and analog output of voltage and frequency.

5.1. Results and discussion

In this study, the accuracy of sensitivity analysis of system stability is theoretically investigated and verified by RTDS. In this case study, an inverter-based resource and a load are connected to the main grid. The inverter is controlled by a droop control system. The scenarios are defined based on the sensitivity analysis. Two scenarios are studied, which are changing control system parameters and load changes. In each scenario, the system performance during a transient three-phase-to-ground fault at the PCC point is investigated.

5.1.1. Transient response to a fault for different load levels

As obtained from numerical analysis, the amount of system load is an important factor in determining the stable transient response of the system during disturbances. By increasing the system load, the system's capability to return to its original steady-state operating point after a transient contingency reduces and can even be a challenging

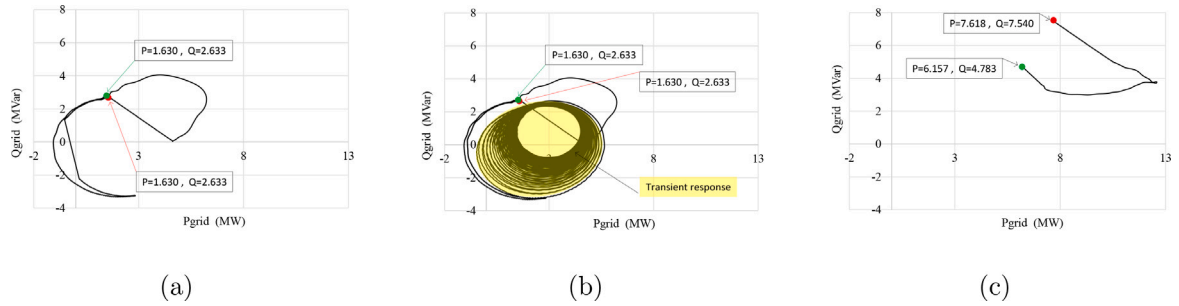

Fig. 7. Transient response of the inverter to a fault. The system with small load: power (a) without and (b) with fluctuations of transient response. The system with large load: power (c) unstable transient response.

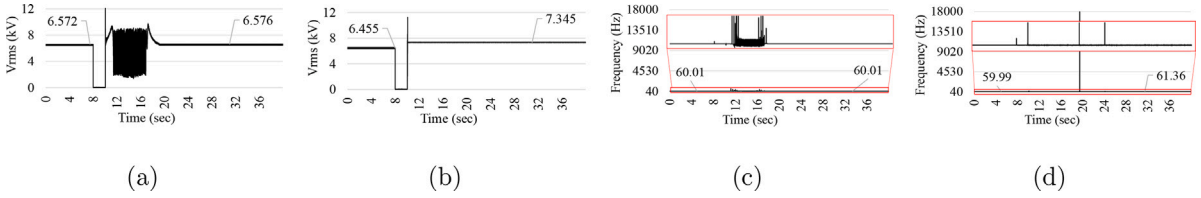

Fig. 8. Transient response of the inverter to a fault. RMS Voltage at PCC in (kV) for (a) small load and (b) large load. Frequency for (c) small load and (d) large load.

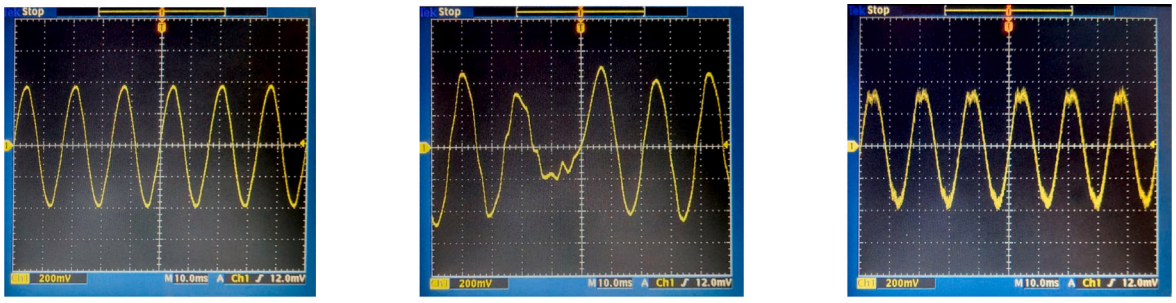

Fig. 9. Transient response of the inverter to a fault for the system with a large load: Phase-A voltage signal from GTAO to Oscilloscope (a) pre-fault (b) during the transient (c) post-fault.

process. This implies that for a larger load, the stability region of the system, known as the domain of attraction, becomes reduced, thereby increasing the likelihood of the disturbance trajectory crossing the system's critical boundary.

Fig. 7-(a) represents the system transient response to a transient three-phase-to-ground fault. The fault will be cleared after 123.7 cycles. This 123.7-cycle fault duration is a critical clearing time for the current system states and conditions, which is defined as the maximum fault duration to guarantee that the system can have a stable transition to the original operating point. If the fault continues over 123.7 cycles, the system becomes unstable. As highlighted in Fig. 7-(a), pre-fault (red point) and post-fault (green point) operating points are the same, and the system returns to its original operating point. The fluctuations of the transient response of the system are excluded from Fig. 7-(a). Fig. 7-(b) highlights the fluctuations of transient response.

By increasing the load in the system with the same parameters, according to numerical analysis, it is expected that the stability region of the system becomes smaller, and for the same fault (three-phase-to-ground with 123.7-cycle duration), the system is incapable of reverting to its initial operational state after clearing the fault. Fig. 7-(c) represents the transient response of the system under the condition of increasing the load at the PCC point. As shown in Fig. 7-(c), the system is unable to revert to its initial steady-state operational position (marked by the red point), resulting in a post-fault steady-state operating point (indicated by the green point) that differs from the pre-fault state. Fig. 8-(a) and (b) represent root-mean-square (RMS) voltages for the case studies with small and large loads, respectively. Comparing the RMS voltages indicates that the voltage at the PCC point increases by 14% in the large load scenarios, and the system loses its voltage stability and it may disconnect from the grid. Moreover, after a three-phase-to-ground fault in the large-load system, the frequency of the system after the transition fluctuates and in the steady-state operation increases to 2.27%, shown in Fig. 8-(d). On the other hand, Fig. 8-(c) represents the frequency of the small-load system after the same fault. The transient response of the system presents a stable transition to the original equilibrium (operating) point. Fig. 9 represents the Hardware-in-the-loop outputs for system transient response to a three-phase fault when the system supplies the large load.

5.1.2. *Transient response to a fault for different voltage control coefficient, $\mathcal{K}_{pv}$*

In a droop control system, voltage and current loop control coefficients need to be selected in an appropriate method. In this study, the effect of choosing a large and small $\mathcal{K}_{pv}$ of voltage loop in droop control on the inverter transient response to a grid-side disturbance is scrutinized. A large $\mathcal{K}_{pv}$ can help the system have a shorter rising time and improve the transient stability of the system after a disturbance. However, it depends on the other part of the system. By increasing the $\mathcal{K}_{pv}$, the system will experience more fluctuation during the transient response. Hence, according to the system condition and the current $\mathcal{K}_{pv}$

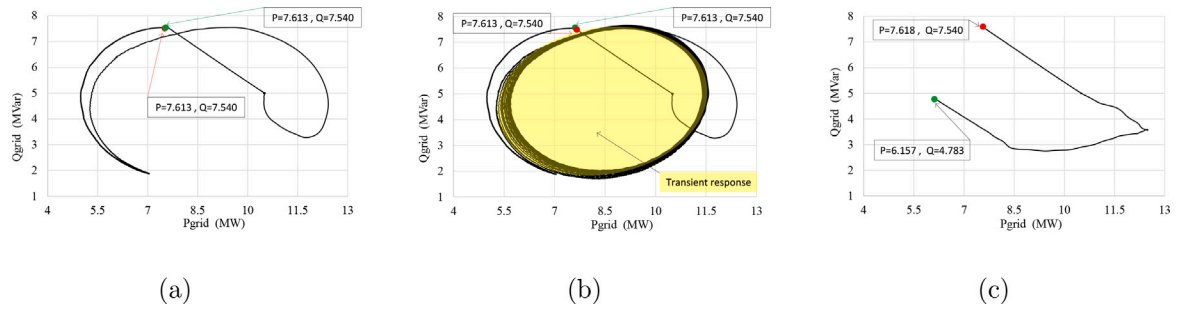

Fig. 10. Transient response of the inverter to a fault. The control system with small $\mathcal{K}_{pv}$: reactive power (a) without and (b) with fluctuations of transient response. The control system with large $\mathcal{K}_{pv}$: reactive power (c) unstable transient response.

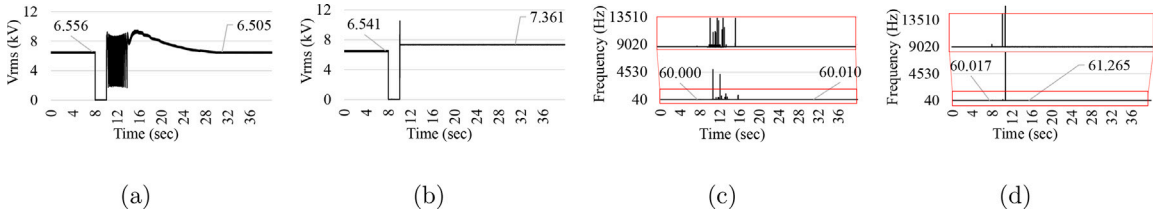

Fig. 11. Transient response of the inverter to a fault: RMS Voltage at PCC in (kV) for (a) small $\mathcal{K}_{pv}$ and (b) large $\mathcal{K}_{pv}$. Frequency for (c) small $\mathcal{K}_{pv}$ and (d) large $\mathcal{K}_{pv}$.

value, increasing or decreasing $\mathcal{K}_{pv}$ can affect the system's transient response and stability during contingencies.

Fig. 10 illustrates the transient response for the system after a three-phase-to-ground fault with a 124-cycle duration for two different $\mathcal{K}_{pv}$ values. As obtained in Section 4.1.3, by increasing $\mathcal{K}_{pv}$, the domain of attraction shrinks, reducing the required time to clear a fault before the system fails. In other words, in this system, decreasing $\mathcal{K}_{pv}$ can reduce the delay in controlling system reaction to applied inputs, improving the system's transient response and system stability during disturbances.

Moreover, the RMS voltages are compared in Fig. 11-(a) and (b), representing a 12.54% increase in the steady-state voltage of the large-$\mathcal{K}_{pv}$ system at post-fault. Fig. 11-(c) and (d) illustrate the system frequency after the fault for the small-$\mathcal{K}_{pv}$ and large-$\mathcal{K}_{pv}$ systems, respectively. The frequency of the large-$\mathcal{K}_{pv}$ system after fault reaches 61.262 Hz, resulting in system frequency instability. On the other hand, choosing a small and appropriate $\mathcal{K}_{pv}$ can help the system to improve the transient stability during the disturbances, shown in Fig. 11-(a) and (c).

6. Conclusion

This paper has developed an HIL-based examination of the stability region in a grid-tied inverter-based resource to scrutinize the sensitivity of inverter dynamic response to a grid-side fault. The RTDS setup and HIL are utilized to authenticate the findings derived from our comprehensive numerical analysis. A stability methodology, the Sum of Squares (SOS)-based technique, and a nonlinear dynamic model are employed to provide a rich, multidimensional perspective on system stability.

The findings are not just theoretical conjectures but are empirically validated, underscoring the potency of numerical analysis as a tool for streamlining and optimizing the scenario assessment process for system stability when paired with a well-suited stability method. We delved into a comparative analysis, pitting the SOS-based Lyapunov method against Krasovskii's method, unearthing discernible distinctions in their efficacy.

In essence, the synergy of HIL-based analysis, the robust RTDS setup, and the intricate numerical analysis rooted in the SOS-based method and nonlinear dynamic model provides actionable insights, and refined tools, and enhances precision in mapping out and understanding the stability perspective of inverter-based resources.

CRediT authorship contribution statement

Hadis Hosseinpour: Writing – review & editing, Writing – original draft, Visualization, Validation, Software, Methodology, Formal analysis, Conceptualization. **Mohammed Ben-Idris:** Writing – review & editing, Supervision, Funding acquisition, Conceptualization.

Declaration of competing interest

The authors declare the following financial interests/personal relationships which may be considered as potential competing interests: Hadis Hosseinpour reports financial support was provided by National Science Foundation. If there are other authors, they declare that they have no known competing financial interests or personal relationships that could have appeared to influence the work reported in this paper.

Data availability

No data was used for the research described in the article.

Acknowledgments

This work has been supported in part by the U.S. National Science Foundation under Grant ECCS-2033927.

References

[1] A. Khodaei, S. Bahramirad, M. Shahidehpour, Microgrid planning under uncertainty, IEEE Trans. Power Syst. 30 (5) (2014) 2417–2425.
[2] A. Hussain, V.-H. Bui, H.-M. Kim, Microgrids as a resilience resource and strategies used by microgrids for enhancing resilience, Appl. Energy 240 (2019) 56–72.
[3] M.M. Mobashsher, R. Keypour, M. Savaghebi, Distributed optimal voltage control in islanded microgrids, Int. Trans. Electr. Energy Syst. 31 (11) (2021) e13045.
[4] M. Mansour-lakouraj, M. Shahabi, Comprehensive analysis of risk-based energy management for dependent microgrid under normal and emergency operations, Energy 171 (2019) 928–943.
[5] K.P. Schneider, F.K. Tuffner, M.A. Elizondo, C.-C. Liu, Y. Xu, D. Ton, Evaluating the feasibility to use microgrids as a resiliency resource, IEEE Trans. Smart Grid 8 (2) (2016) 687–696.

[6] Z. Shuai, Y. Sun, Z.J. Shen, W. Tian, C. Tu, Y. Li, X. Yin, Microgrid stability: Classification and a review, Renew. Sustain. Energy Rev. 58 (2016) 167–179.
[7] Y. Yan, D. Shi, D. Bian, B. Huang, Z. Yi, Z. Wang, Small-signal stability analysis and performance evaluation of microgrids under distributed control, IEEE Trans. Smart Grid 10 (5) (2018) 4848–4858.
[8] N. Asadi, M. Hamzeh, K. Abbaskhanian, The impact of DSTATCOM on the small-signal stability of islanded microgrids, in: 2020 11th Power Electronics, Drive Systems, and Technologies Conference, PEDSTC, IEEE, 2020, pp. 1–7.
[9] S. Satapathy, N. Nahak, A real time integrated modelling and control of modified pumped storage governor-PSS damping action for random renewable penetration, e-Prime - Adv. Electr. Eng. Electron. Energy 7 (2024) 100429, http://dx.doi.org/10.1016/j.prime.2024.100429.
[10] S. Wang, J. Su, X. Yang, Y. Du, Y. Tu, H. Xu, A review on the small signal stability of microgrid, in: 2016 IEEE 8th International Power Electronics and Motion Control Conference, IPEMC-ECCE Asia, IEEE, 2016, pp. 1793–1798.
[11] M. Kabalan, P. Singh, D. Niebur, A design and optimization tool for inverter-based microgrids using large-signal nonlinear analysis, IEEE Trans. Smart Grid 10 (4) (2018) 4566–4576.
[12] H. Hosseinpour, M. MansourLakouraj, M. Ben-Idris, H. Livani, Large-signal stability analysis of inverter-based microgrids via sum of squares technique, in: 2023 IEEE Texas Power and Energy Conference, TPEC, IEEE, 2023, pp. 1–6.
[13] B. She, J. Liu, F. Qiu, H. Cui, N. Praisuwanna, J. Wang, L.M. Tolbert, F. Li, Systematic controller design for inverter-based microgrids with certified large-signal stability and domain of attraction, IEEE Trans. Smart Grid (2023).
[14] Z. Meng, H. Xu, P. Ge, J. Hu, Large-signal modeling and stable region estimation of DC microgrid with virtual DC machine control, Int. J. Electr. Power Energy Syst. 151 (2023) 109122.
[15] Y. Du, Y. Men, L. Ding, X. Lu, Large-signal stability analysis for inverter-based dynamic microgrids reconfiguration, IEEE Trans. Smart Grid (2021).
[16] H. Hosseinpour, M. MansourLakouraj, M. Ben-Idris, H. Livani, Large-signal stability analysis of inverter-based AC microgrids: A critical and analytical review, IEEE Access (2023).
[17] D. Espín-Sarzosa, R. Palma-Behnke, C.A. Cañizares, U. Annakkage, M. Elizondo, E. Espina, W. Du, M. Kaba-lan, L. Meegahapola, P.A. Mendoza-Araya, et al., Microgrid modeling for stability analysis, IEEE Trans. Smart Grid (2023).
[18] M. Naderi, Y. Khayat, Q. Shafiee, F. Blaabjerg, H. Bevrani, Dynamic modeling, stability analysis and control of interconnected microgrids: A review, Appl. Energy 334 (2023) 120647.
[19] D. Pal, B.K. Panigrahi, B. Johnson, D. Venkatramanan, S. Dhople, Large-signal stability analysis of three-phase grid-following inverters, IEEE Trans. Energy Convers. (2023).
[20] Z. Duan, Y. Meng, Y. Duan, H. Zhang, X. Wang, X. Wang, Large-signal stability analysis and enhancement of modular multilevel matrix converter under power fluctuation based on TS fuzzy model theory, IEEE Trans. Power Electron. (2023).
[21] Y. Zhang, H. Zheng, C. Zhang, X. Yuan, W. Xiong, Y. Cai, TS fuzzy model based large-signal stability analysis of DC microgrid with various loads, IEEE Access (2023).
[22] M. Kabalan, P. Singh, D. Niebur, Large signal Lyapunov-based stability studies in microgrids: A review, IEEE Trans. Smart Grid 8 (5) (2016) 2287–2295.
[23] S. Liu, X. Li, M. Xia, Q. Qin, X. Liu, Takagi-Sugeno multimodeling-based large signal stability analysis of DC microgrid clusters, IEEE Trans. Power Electron. 36 (11) (2021) 12670–12684.
[24] J. Jiang, F. Liu, S. Pan, X. Zha, W. Liu, C. Chen, L. Hao, A conservatism-free large signal stability analysis method for DC microgrid based on mixed potential theory, IEEE Trans. Power Electron. 34 (11) (2019) 11342–11351.
[25] M.M. Mobashsher, A.A. Abdoos, S.M. Hosseini, S.M. Hashemi, M. Sanaye-Pasand, A new fault type classification method in the presence of inverter-based resources, Int. J. Electr. Power Energy Syst. 147 (2023) 108793.
[26] M.M. Mobashsher, S.M. Hosseini, A.A. Abdoos, S.M. Hashemi, M. Sanaye-Pasand, H. Mehrjerdi, A new fault location scheme based on local measurements for transmission lines connected to inverter-based resources, Electr. Power Syst. Res. 228 (2024) 110079.
[27] W. Xie, M. Han, W. Cao, J.M. Guerrero, J.C. Vasquez, System-level large-signal stability analysis of droop-controlled DC microgrids, IEEE Trans. Power Electron. 36 (4) (2020) 4224–4236.
[28] Z. Zhang, X. Yang, S. Zhao, D. Wu, J. Cao, M. Gao, G. Zeng, Z. Wang, Large-signal stability analysis of islanded DC microgrids with multiple types of loads, Int. J. Electr. Power Energy Syst. 143 (2022) 108450.
[29] D. Marx, P. Magne, B. Nahid-Mobarakeh, S. Pierfederici, B. Davat, Large signal stability analysis tools in DC power systems with constant power loads and variable power loads—A review, IEEE Trans. Power Electron. 27 (4) (2011) 1773–1787.
[30] H. Hosseinpour, M. MansourLakouraj, M. Ben-Idris, H. Livani, Lyapunov-based large-signal stability analysis of inverter-based microgrids, in: 2022 North American Power Symposium, NAPS, IEEE, 2022, pp. 1–6.
[31] F. Andrade, K. Kampouropoulos, L. Romeral, J.C. Vasquez, J.M. Guerrero, Study of large-signal stability of an inverter-based generator using a Lyapunov function, in: IECON 2014-40th Annual Conference of the IEEE Industrial Electronics Society, IEEE, 2014, pp. 1840–1846.
[32] N. Monshizadeh, F. Mancilla-David, R. Ortega, R. Cisneros, Nonlinear stability analysis of the classical nested PI control of voltage sourced inverters, IEEE Control Syst. Lett. 6 (2021) 1442–1447.
[33] D. Karimipour, F.R. Salmasi, Stability analysis of AC microgrids with constant power loads based on Popov's absolute stability criterion, IEEE Trans. Circuits Syst. II 62 (7) (2015) 696–700.
[34] R. Debnath, G. Gupta, D. Kumar, Lyapunov-Krasovskii passivity based stability analysis of grid-tied inverters, Int. J. Electr. Power Energy Syst. 143 (2022) 108460.
[35] M.M. Mobashsher, A.A. Abdoos, S.M. Hosseini, S.M. Hashemi, M. Sanaye-Pasand, An accelerated distance protection scheme for the lines connected to inverter-based resources, IEEE Syst. J. 17 (4) (2023) 6272–6281.
[36] A. Hooshyar, E.F. El-Saadany, M. Sanaye-Pasand, Fault type classification in microgrids including photovoltaic DGs, IEEE Trans. Smart Grid 7 (5) (2015) 2218–2229.
[37] W. Tan, A. Packard, Stability region analysis using sum of squares programming, in: 2006 American Control Conference, IEEE, 2006, p. 6.
[38] N. Pogaku, M. Prodanovic, T.C. Green, Modeling, analysis and testing of autonomous operation of an inverter-based microgrid, IEEE Trans. Power Electron. 22 (2) (2007) 613–625.
[39] P.A. Parrilo, Polynomial games and sum of squares optimization, in: Proceedings of the 45th IEEE Conference on Decision and Control, IEEE, 2006, pp. 2855–2860.
[40] C. Mishra, A. Pal, J.S. Thorp, V.A. Centeno, Transient stability assessment of prone-to-trip renewable generation rich power systems using Lyapunov's direct method, IEEE Trans. Sustain. Energy 10 (3) (2019) 1523–1533.
[41] R. Furqon, Y.-J. Chen, M. Tanaka, K. Tanaka, H.O. Wang, An SOS-based control Lyapunov function design for polynomial fuzzy control of nonlinear systems, IEEE Trans. Fuzzy Syst. 25 (4) (2016) 775–787.
[42] K.K. Hassan, et al., Nonlinear Systems, Departement of Electrical and Computer Engineering, Michigan State University, 2002.
[43] A. Papachristodoulou, J. Anderson, G. Valmorbida, S. Prajna, P. Seiler, P.A. Parrilo, SOSTOOLS: Sum of squares optimization toolbox for MATLAB, 2013, Available from http://www.mit.edu/~parrilo/sostools.
[44] O. Kwon, M.-J. Park, J.H. Park, S.-M. Lee, Improvement on the feasible region of H_∞ performance and stability for systems with interval time-varying delays via augmented Lyapunov–Krasivskii functional, J. Franklin Inst. 353 (18) (2016) 4979–5000.